JOURNAL OF COMPUTATIONAL PHYSICS 35, 12–35 (1980)

Open Boundary Conditions in Rotating Fluids*

ALEJANDRO L. CAMERLENGO AND JAMES J. O'BRIEN

Mesoscale Air–Sea Interaction Group, Florida State University, Tallahassee, Florida 32306

Received August 17, 1978; revised May 9, 1979

Outflow radiation conditions have frequently been used at open boundaries in oceanography and meteorology. A new implementation of Orlanski's formulation for problems requiring a radiation open boundary has been developed. Three different cases in which Rossby and Kelvin waves are present are studied. In all these tests the proposed open boundary condition shows no reflection at the outflow of the Kelvin wave. However, some reflection at the outflow of the Rossby wave is observed.

1. INTRODUCTION

This paper seeks to give some insight into the role open boundary conditions play in the numerical simulation of geophysical fluid motion. The question we seek to answer is: In what way can we accurately simulate the outflow of Rossby and Kelvin waves from a domain with open boundaries?

Fine-mesh grids are used to achieve an adequate resolution in meteorological problems. The domain to be modelled has to satisfy the constraints imposed by the computer speed and capacity. For this reason, fluids with open boundaries have to be considered in order to achieve the physically desired resolution.

An open boundary condition is a computational boundary that allows phenomena generated in the interior domain to pass through the artificial boundary without distortion and without affecting the interior solution. The study of this problem is of fundamental importance in fluid dynamics. This is especially true in the areas of oceanography (ocean circulation, eddies, etc.) and meteorology (convection, weather prediction, air pollution modelling, etc.). Background references are Haltiner [5] for meteorology and Reid *et al.* [15] for oceanography. The importance of open boundary conditions has been recognized since the beginnings of the computer era. The first realistic study was made by Charney *et al.* [1], when they studied the limited-area integration of the barotropic vorticity equation. They computed the vorticity at outflow boundaries by a linear extrapolation formula and specified the vorticity at inflow boundaries. Unfortunately, the extrapolation formula they used to compute the vorticity caused the scheme to become unstable (Platzman, [14]).

Nitta [10] and Matsuno [8] specified the outflow boundary conditions by extrapolating the interior solution to the boundary. However, improper extrapolations

* Contribution No. 0150 of the Geophysical Fluid Dynamics Institute, Florida State University.

0021-9991/80/040012–24$02.00/0

tended to cause numerical instabilities in the solutions. Hill (1968) integrated a two-level baroclinic model over a series of nested grids in such a way that the final grid size was as small as desired. Wang and Halpern [17] obtained conditions for a limited area barotropic primitive equation model from a coarse-mesh hemispheric model. This study revealed the generation of small-scale spatial oscillations in the interior solution. These oscillations may not be attributed to numerical instabilities (Shapiro and O'Brien [16]), but rather to the overspecification of the boundary conditions. In order to suppress these oscillations, an artificial diffusion coefficient is introduced. The trouble is that the larger this coefficient, the smoother the interior solution, with a consequent distortion of the physical modes. In other words, the viscosity removes the small scale flow which the fine mesh is designed to handle and the solution may be more unrealistic than a coarse-grid model in a closed domain without open boundaries.

As the computational models become more sophisticated, the problem of specifying the correct boundary becomes more critical. For this reason, this problem is attracting considerable interest in the scientific community.

A more practical and realistic formulation is the work of Orlanski [13]. He used Sommerfeld radiation conditions for problems requiring a prescribed open boundary. The equations he used were, of course, hyperbolic in nature. He integrated two models to demonstrate the applicability of his set of open boundary conditions: the collapsing bubble and the spatially growing Kelvin–Helmholtz instability. An ingenious method that minimizes the computational (artificial) reflections which occur at the boundaries, has been developed by Engquist and Majda [4]. However, as the scope of the present research is focussed in open boundary conditions and not on absorbing boundary conditions, their particular method is not implemented.

Our principal interest is rotating stratified fluid models of the atmosphere and ocean. In particular, we are interested in solutions which contain Rossby waves as an important mechanism. Our intention is to investigate a set of open boundary conditions in which these waves are present. There are many model problems which one can choose, but in numerical experimentation, one would like to address a pertinent problem which at the same time has only few degrees of freedom. By separating the equations of motion into vertical modes, we can reduce the number of degrees of freedom in the vertical to one. For a set of open boundary conditions to work for a non-linear problem, it is essential that they must also satisfy the linear problem. Thus, we restrict our initial examination to the linear case.

Additional wave modes can be excited because of the fact that the Coriolis acceleration is zero at the equator. For this reason, the equatorial case was chosen. If we consider the set of primitive equations on an equatorial β-plane, it is straightforward to design a problem in which the Rossby, gravity, and Kelvin waves are present. Following Moore [9] it is possible to excite these waves with a variety of forcing functions. We run a series of experiments exciting these waves and studying their propagation in a basin in which one of the boundaries is not a rigid wall.

This investigation studies the evolution of Rossby and Kelvin waves through a set of open boundaries and also addresses the free and forced wave problem in three experiments. A new simple implementation of Orlanski's scheme is rather useful.

In the methods considered in this study, the local phase speed close to the boundary is evaluated for each variable. If the local phase speed is positive, an outflow condition is extrapolated from the interior solution according to the Sommerfeld radiation condition. On the other hand, if the local phase speed is negative, an inflow condition is specified. It is not correct to state that these methods overspecify the solution at inflow points, or underspecify the solution at outflow points. A local adjustment allows non-dispersive or dispersive waves which are well-resolved to propagate from the interior domain through the boundary.

2. The Model

Let us consider the linear shallow-water wave equations on an equatorial β-plane. For a model consisting of two layers of density, ρ_i, and depth, H_i ($i = 1, 2$ for upper and lower layers, respectively) there are two vertical modes. The barotropic wave modes are characterized by a very large propagational speed compared with that of the baroclinic wave modes. Assuming that the lower layer is infinitely deep ($H_2 \gg H_1$), will allow us to consider it of constant density and at rest for all x, y and t. With this constraint, we automatically filter out the barotropic mode of motion.

If we do not consider turbulent mixing between the ocean layers, i.e., ρ_1 being a constant, we can define the reduced gravity, g', as:

$$g' = \frac{\rho_2 - \rho_1}{\rho_2} g. \tag{2.1}$$

With these assumptions, the forced linear shallow-water wave equations for the first baroclinic mode can be written as follows:

$$\begin{aligned} \frac{\partial u}{\partial t} &= \beta y v - g' \frac{\partial h}{\partial x} + A \nabla^2 u + \tau^x/\rho H \\ \frac{\partial v}{\partial t} &= -\beta y u - g' \frac{\partial h}{\partial y} + A \nabla^2 v + \tau^y/\rho H \\ \frac{\partial h}{\partial t} &= -H \left(\frac{\partial u}{\partial x} + \frac{\partial v}{\partial y} \right). \end{aligned} \tag{2.2}$$

The parameters for these case studies are: $A = 10^2$ m^2 sec^{-1}, $g' = 2.10^{-2}$ m sec^{-2}, $H = 200$ m and $\beta = 2.10^{-11}$ m^{-1} sec^{-1}.

It is convenient to non-dimensionalize the equations. Let C be the scaling velocity for u and v. Let L_x and L_y be the horizontal and meridional length scales, respectively. Let T be the characteristic time scale, and H, the characteristic height scale. We then introduce the nondimensional variables, denoted by primes, as follows:

$$\begin{aligned}(u, v) &= C(u', v')\\ x &= L_x x'\\ y &= L_y y'\\ h &= Hu'\\ t &= Tt'.\end{aligned} \tag{2.3}$$

The appropriate scaling is: $L_x = C/\beta W$ (where W is the width of the basin), internal radius of deformation (x-scale); $L_y = (C/\beta)^{1/2}$, equatorial radius of deformation (y-scale); $C = (g'H)^{1/2}$, phase speed of the first baroclinic mode; and $T = (\beta L_y)^{-1}$, characteristic time scale.

The nondimensional coordinates, x and y, and the corresponding velocity components, u and v, are positive eastward and northward. The nondimensional forms of Eqs. (2.2) yield:

$$\begin{aligned}\frac{\partial u}{\partial t} &= yv - \alpha\frac{\partial h}{\partial x} + A'\left(\alpha^2\frac{\partial^2 u}{\partial x^2} + \frac{\partial^2 u}{\partial y^2}\right) + \delta(\tau^x/\rho)\\ \frac{\partial v}{\partial t} &= -yu - \frac{\partial h}{\partial y} + A'\left(\alpha^2\frac{\partial^2 v}{\partial x^2} + \frac{\partial^2 v}{\partial y^2}\right) + \delta(\tau^y/\rho)\\ \frac{\partial h}{\partial t} &= -\left(\alpha\frac{\partial u}{\partial x} + \frac{\partial v}{\partial y}\right).\end{aligned} \tag{2.4}$$

Primes have been dropped from the nondimensional quantities. The nondimensional parameters, α, δ, and A', have been naturally introduced into the dimensionless mathematical problem.

With the particular scaling used in our experiments, it can be deduced that:

$$\alpha = W/L_a \tag{2.5}$$

$$\delta = aH^{-7/4} \tag{2.6}$$

$$A' = bH^{-3/4} \tag{2.7}$$

where the constants a and b, are defined as:

$$a = (g')^{1/4}\beta^{-1/2} \tag{2.8}$$

$$b = A\beta^{1/2}(g')^{-3/4}. \tag{2.9}$$

When the equivalent depth, H, increases (decreases), the coefficients A' and δ will tend to decrease (increase). The contribution of A' is almost negligible, due to the small lateral eddy viscosity chosen in our problem. Moreover, the value of α will depend on the number of internal equatorial Rossby radii of deformation contained in the width of the basin.

Comparing the three nondimensional parameters, it is obvious that δ is the leading term by two or three orders of magnitude. The role of δ, the most important nondimensional parameter, is to excite the free and forced waves. Because of the linearity

of the problem under consideration, the waves cannot grow in amplitude, and the size of the forcing is rather arbitrary. Furthermore, the boundary conditions will not depend on the size of δ.

From these results it can be concluded that the three nondimensional parameters play no important role in the physics of the problem. For this reason, this is an ideal problem for testing different sets of open boundary conditions.

The model geometry is a rectangular flat-bottomed ocean. Its southern boundary extends 25 internal radii of deformation along the equator ($L = 25L_x$), while its meridional boundary extends 5 equatorial radii of deformation in the north-south direction ($W = 5L_y$). Although the width of the basin does not play any fundamental role in this study, the particular length scale chosen in the x direction will give us a good resolution of the trapped coastal Kelvin wave travelling along the eastern boundary. On the other hand, the choice of the length scale in the y direction ensures a good resolution of the trapped equatorial Kelvin (coastal Kelvin) wave travelling along the southern (northern) boundary. In the different experiments to be conducted, the boundaries will be solid walls of zero slip or open boundaries. In the next section, we will discuss the different sets of open boundary conditions in further detail.

A staggered grid in space is used to avoid the noise produced by the high wave numbers. The grid is also staggered in time to reduce the amount of computer work involved when solving these equations. This staggered grid in space and time can be considered as the superposition of two elementary subgrids (Fig. 1). The truncation

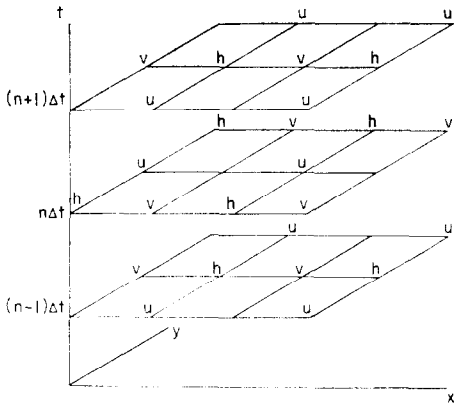

FIG. 1. Description of the height, zonal, and meridional velocity for both lattices.

error and the computational modes are the same as in the non-staggered grid. Let the continuous variables be replaced by the discrete variables j, k, and n. These new variables are defined by the relations:

$$\begin{aligned} x &= j\,\Delta x \\ y &= k\,\Delta y \\ t &= n\,\Delta t \end{aligned} \tag{2.10}$$

where Δx, Δy and Δt are the finite-difference intervals with respect to space (i.e., x and y) and time.

A leapfrog scheme in time and a centered space difference are applied for all x and y derivatives in the system. The leapfrog scheme has the property of introducing no computational damping of the physical solutions of the system.

The representation of the velocity and height fields in the time-space domain will then be:

$$\begin{aligned} h^{n'}_{jk} &= h'((j-1/2)\,2\Delta x, (k-1/2)\,2\Delta y, n\,\Delta t) \\ u^{n'}_{jk} &= u'((j-3/2)\,2\Delta x, (k-1)\,2\Delta y, n\,\Delta t) \\ v^{n'}_{jk} &= v'((j-1)\,2\Delta x, (k-3/2)\,2\Delta y, n\,\Delta t) \\ h^{n}_{jk} &= h((j-1)\,2\Delta x, (k-1)\,2\Delta y, n\,\Delta t) \\ u^{n}_{jk} &= u((j-1)\,2\Delta x, (k-3/2)\,2\Delta y, n\,\Delta t) \\ v^{n}_{jk} &= v((j-3/2)\,2\Delta x, (k-1)\,2\Delta y, n\,\Delta t) \end{aligned} \tag{2.11}$$

where the primed quantities correspond to variables defined at odd time levels.

The staggered grid in space and time is constructed in such a way that the variables u', v, and h, are defined at the equator (southern boundary), which will be symmetric during the whole experiment. However, because the viscous terms have to be computed an extra row of velocity variables has to be defined outside the physical boundary. The value of the velocity outside the domain is determined by applying the no-slip condition at the boundary.

The time step of $\Delta t = 1/28$, used in this study, will satisfy the CFL stability criterion. The values of $\Delta x = L_x/4$ and $\Delta y = L_y/15$ will give us a good resolution of the boundary layers associated with both the coastal and equatorial Kelvin waves, respectively.

In numerical modelling of geophysical systems, the application of a realistic forcing function to the governing equations is of critical importance. The model is started from rest by applying an easterly wind stress of the form $\tau^y = 0$, $(\tau^x/\rho) = T(t)\,G(x)$, where

$$T(t) = \tanh(n\,\Delta t) - \tanh((n-m)\,\Delta t) - 1 \tag{2.12}$$

$$G(x) = -B/[1 + \exp(\gamma(x - x_0))]. \tag{2.13}$$

In our case, $\gamma = 2$, $x_0 = L/3$, $B = 0.1$, and m is equal to $4/\Delta t$ ($15/\Delta t$) for the first (the other) experiment(s).

Figure 2a represents the function $G(x)$ for the first two experiments. This figure shows that a uniform easterly wind stress is applied to the western third $L/3$ of the basin. For the third experiment, the function $G(x)$ is set equal to a constant (-0.1 N m^{-2}) during the whole period of integration of all grid points.

Figure 2b represents the function $T(t)$ for the second and third experiments. For the first case, the uniform easterly wind is maintained until time 4.0, at which time the

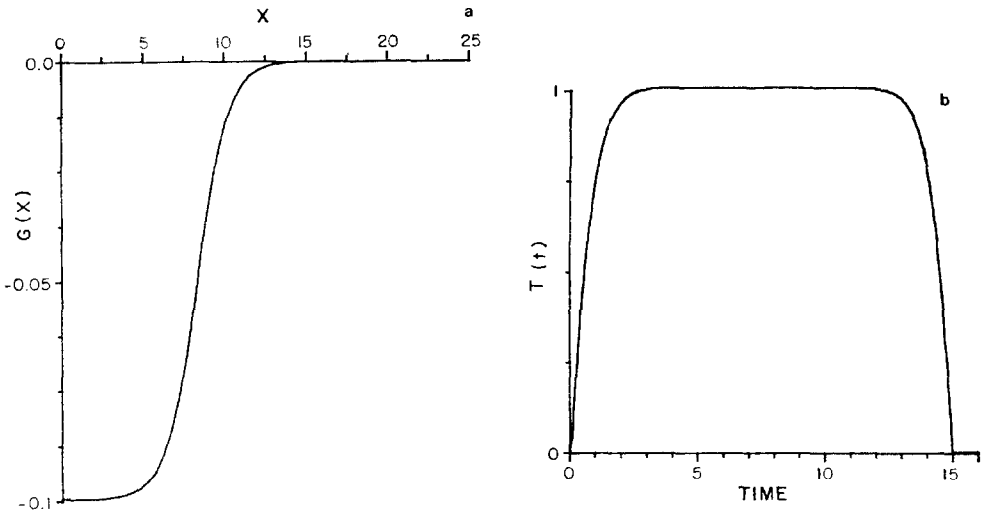

FIG. 2. Illustration of the functions: (a) $G(x)$, for the free wave problem; and (b) $T(t)$ for $m = 15/\Delta t$.

equatorial Kelvin wave, fully developed, is in the middle of the basin, travelling towards the eastern boundary (Figs. 5a,b, and c). Zero wind stress forcing is maintained from time 4.0 to the end of the model integration, at time 12.0. For the other two experiments, while the function $G(x)$ differs (as we have discussed above), the easterly wind is maintained to the end of the model integration. With the initial conditions, $u^0_{jk} = v^0_{jk} = h^0_{jk} = 0$, for all grid points, this results in $v^1_{jk} = h^1_{jk} = 0$, and $u^1_{jk} = \Delta t(\partial u/\partial t)^0_{jk} = \Delta t(\tau^x/\rho H)$.

3. Open Boundary Conditions

The shallow-water wave equations are hyperbolic in nature. The most accurate way to prescribe the outflow at a certain boundary for the hyperbolic system is to use at the boundary a Sommerfeld radiation condition:

$$\frac{\partial \psi}{\partial t} + F\frac{\partial \psi}{\partial x} = 0 \tag{3.1}$$

where ψ is any variable, and F, the phase speed. There are many methods for implementing (3.1). The experiments here are conducted using the open boundary conditions from Orlanski [13]. In addition, a modified version of Orlanski's boundary condition is implemented.

Boundary Condition I: *Orlanski's Method*

In this method the phase speed is numerically evaluated for the interior points close

to the open boundary. By using a leapfrog representation of Eq. (3.1) for each variable, the evaluated phase speed, F_ψ, yields:

$$\left(\frac{\psi^n_{B-1} - \psi^{n-2}_{B-1}}{2\Delta t}\right) + F_\psi \left[\left(\frac{\psi^n_{B-1} + \psi^{n-2}_{B-1}}{2}\right) - \psi^{n-1}_{B-2}\right] \frac{1}{\Delta x} = 0 \tag{3.2}$$

where the index, B, denotes a point at the boundary, $B-1$, the first interior point, etc. In other words, values of ψ near the boundary and previous in time are used to estimate F_ψ for each variable at each time step. Equation (3.1) is used again to evaluate the extrapolated value of ψ^{n+1}_B as a function of F. The final formulation for the phase speed then is:

$$\begin{aligned} F_\psi &= 0 && \text{if } F_\psi \leqslant 0 \\ F_\psi &= \frac{\Delta x}{\Delta t} && \text{if } F_\psi > \Delta x/\Delta t \\ F_\psi &= -\psi_t/\psi_x && \text{if } 0 < F_\psi < \Delta x/\Delta t \end{aligned} \tag{3.3}$$

where the approximation (3.2) is implied. However, because a staggered grid in space and time is used, the specific numerical formulation of F_ψ is slightly different at different boundaries. Equation (3.4) represents the numerical evaluation of the phase speed at the northern boundary while Eq. (3.13) represents the evaluation of F_ψ at the western boundary.

Boundary Condition II: *Variation of Orlanski's Method*

A new formulation, involving a variation of Orlanski's condition, is tested. In this formulation, the local phase speed, F_ψ, is evaluated as suggested by Orlanski but with the following difference: when the local phase speed is outward (inward), an outflow (inflow) boundary condition is prescribed. The outflow (inflow) boundary condition is set equal to $\Delta x/\Delta t$ (zero) for western open boundary, and $\Delta y/\Delta t$ (zero) for a northern open boundary. These two cases are represented by Eqs. (3.8) and (3.10), respectively.

This variation of Orlanski's boundary condition is somewhat arbitrary, but because of the lack of a practical theoretical guidance, a pragmatic approach is adopted.

Three experiments are conducted by using the open boundary conditions outlined above. As a consequence, different solutions are obtained for each set of open boundary conditions. The ideal solution is one in which the interior flow is essentially identical to the solution in a larger enclosed basin, i.e., a minimum distortion of the interior flow.

In the first experiment, the northern boundary is open, and the staggered grid is implemented in such a way that the variable, ψ, has the values of v, u', h at the northern boundary. The numerical evaluation of the phase speed following Orlanski's method yields to:

$$F_\psi = -\left(\frac{E^n_{i,B} - E^{n-2}_{i,B}}{E^n_{i,B} + E^{n-2}_{i,B} - D^n_{i,B} - D^{n-2}_{i,B}}\right) \cdot \frac{2\Delta y}{\Delta t} \tag{3.4}$$

where

$$E_{i,B} = (\psi_{i-1,B-1} + \psi_{i+1,B-1})/2 \tag{3.5}$$

$$D_{i,B} = (\psi_{i-1,B-3} + \psi_{i+1,B-3})/2 \tag{3.6}$$

and i denotes an arbitrary grid point in the x direction. The extrapolated value of $\psi_{i,B}^{n+1}$ then is:

$$\psi_{i,B}^{n+1} = \frac{[1 - F_\psi(\Delta t/\Delta y)]\, \psi_{i,B}^{n-1} + 2F_\psi E_{i,B}^{n}(\Delta t/\Delta y)}{1 + F_\psi(\Delta t/\Delta y)}. \tag{3.7}$$

In the new implementation of Orlanski's method, the value of $\psi_{i,B}^{n+1}$ is:

$$\begin{aligned} \psi_{i,B}^{n+1} &= E_{i,B}^{n} \text{ at the outflow points.} \\ &= \psi_{i,B}^{n-1} \text{ at the inflow points.} \end{aligned} \tag{3.8}$$

Equation (3.8) can be looked upon as a zeroth order approximation to Eq. (3.1) as opposed to Orlanski's first order approximation (Eq. (3.7)). Figure 3 shows the representation of the variable, ψ, in the $x - y$ plane for these methods.

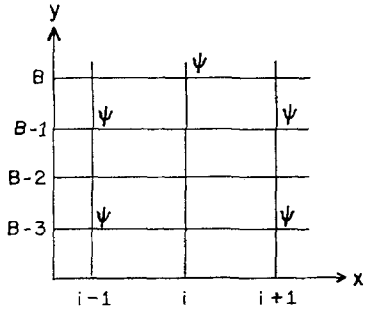

FIG. 3. Representation of an arbitrary variable Ψ in the (x, y) plane for Orlanski's method and the new implementation applied to a northern boundary condition.

In the last two experiments, the integration of the model is started in a closed domain. After a certain time, an open boundary is implemented in the middle of the basin, and the time integration is continued in the eastern half of the basin. As the physics of these two experiments differ, the times in which we decide to place our set of new boundary conditions are also different. The open boundary is implemented in such a way that the variable, ψ, has the value of u, v', and h at that boundary.

Following the same procedure outlined before, the extrapolated variable, $\psi_{B,W}^{n+1}$ (where W denotes an arbitrary grid point in the y direction), has a value of:

$$\psi_{B,W}^{n+1} = \frac{(1 - F_\psi(\Delta t/\Delta x))\, \psi_{B,W}^{n-1} + 2P_{B,W}^{n}(\Delta t/\Delta x)}{1 + F_\psi(\Delta t/\Delta x)} \tag{3.9}$$

in the Orlanski method;

$$\begin{aligned}\psi_{B,W}^{n+1} &= P_{B,W}^{n} \text{ at the outflow points} \\ &= \psi_{B,W}^{n-1} \text{ at the inflow points}\end{aligned} \tag{3.10}$$

in the new implementation of Orlanski's method, where

$$P_{B,W} = (\psi_{B-1,W-1} + \psi_{B-1,W+1})/2. \tag{3.11}$$

$$R_{B,W} = (\psi_{B-3,W-1} + \psi_{B-3,W+1})/2. \tag{3.12}$$

The value of F_ψ is:

$$F_\psi = -\frac{P_{B,W}^{n} - P_{B,W}^{n-2}}{P_{B,W}^{n} + P_{B,W}^{n-2} - R_{B,W}^{n} - R_{B,W}^{n-2}} \cdot \frac{2\Delta x}{\Delta t}. \tag{3.13}$$

Figure 4 shows the representation of the variable, ψ, in the y, t plane for these methods.

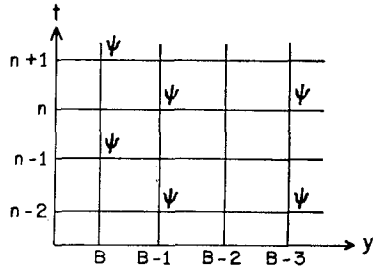

FIG. 4. Representation of an arbitrary variable Ψ in the (y, t) plane for Orlanski's method and the new implementation applied to a western boundary condition.

4. RESULTS

In the first experiment at time $t = 0$, we impose an easterly wind in the western third of the basin, up to time 4.0 (Eqs. (2.12) and (2.13)). The east–west stress is zero in the remaining two-thirds of the basin, while the north–south stress is zero everywhere. This impulsive wind stress excites an internal equatorial Kelvin wave, which travels eastward along the equator. After reaching the eastern boundary, this wave travels poleward along that boundary.

This first experiment is designed in such a way that the outflow of an isolated nondispersive wave can be studied in full detail. In this case, the nondispersive wave is the eastern coastal Kelvin wave. A first run in a closed basin of solid walls of zero slip preceeded the experiments with the northern open boundary.

The closed basin solution (Figs. 5a, b, and c) shows the equatorial Kelvin wave in the middle of the basin along the equator. The velocity, u, associated with this

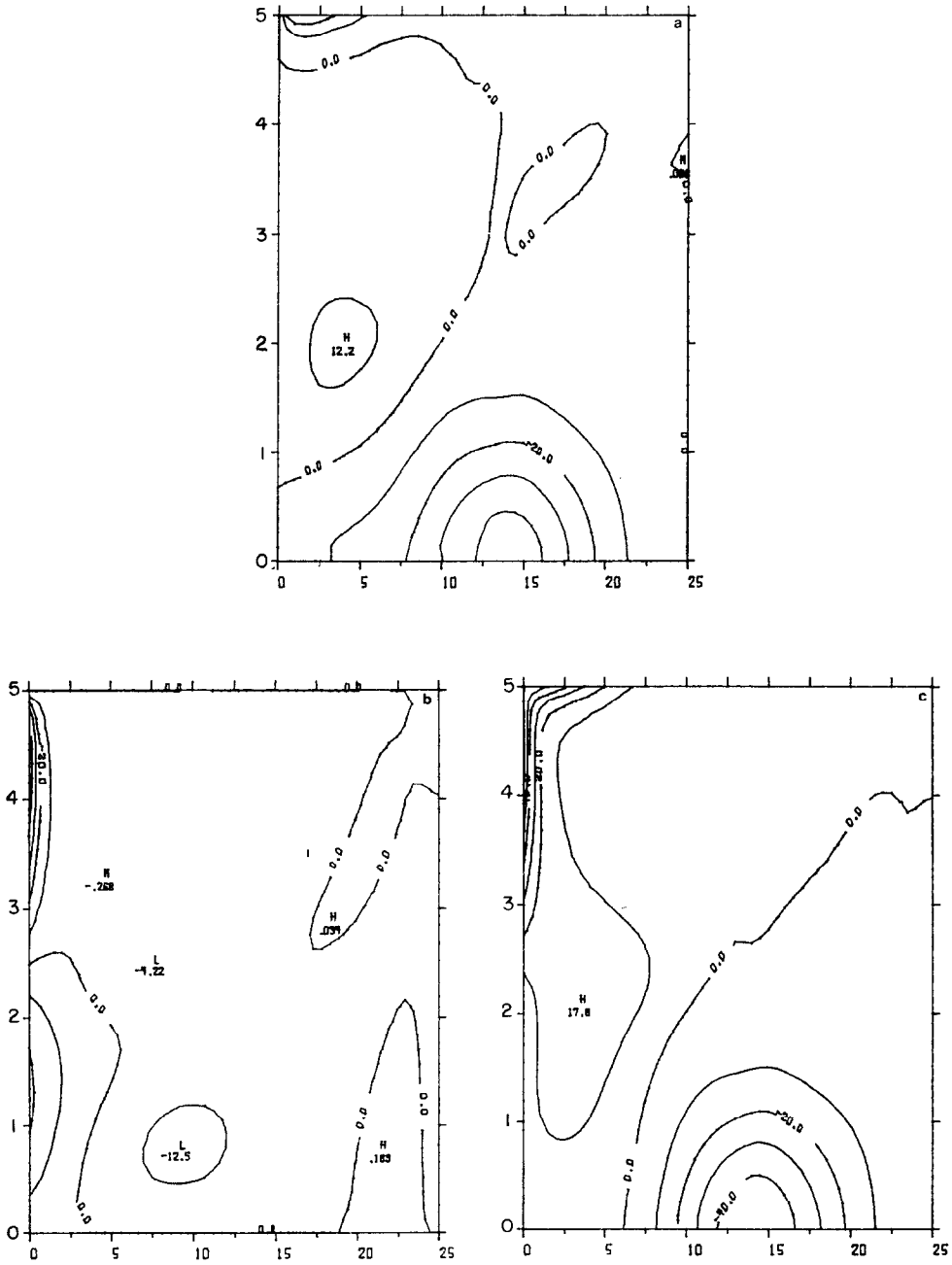

FIG. 5. (a) Zonal velocity, (b) meridional velocity, and (c) height fields at time 4.0, for the closed domain, for the first experiment. The plotting frequency is 1000 units of dimensionless velocity and height, respectively.

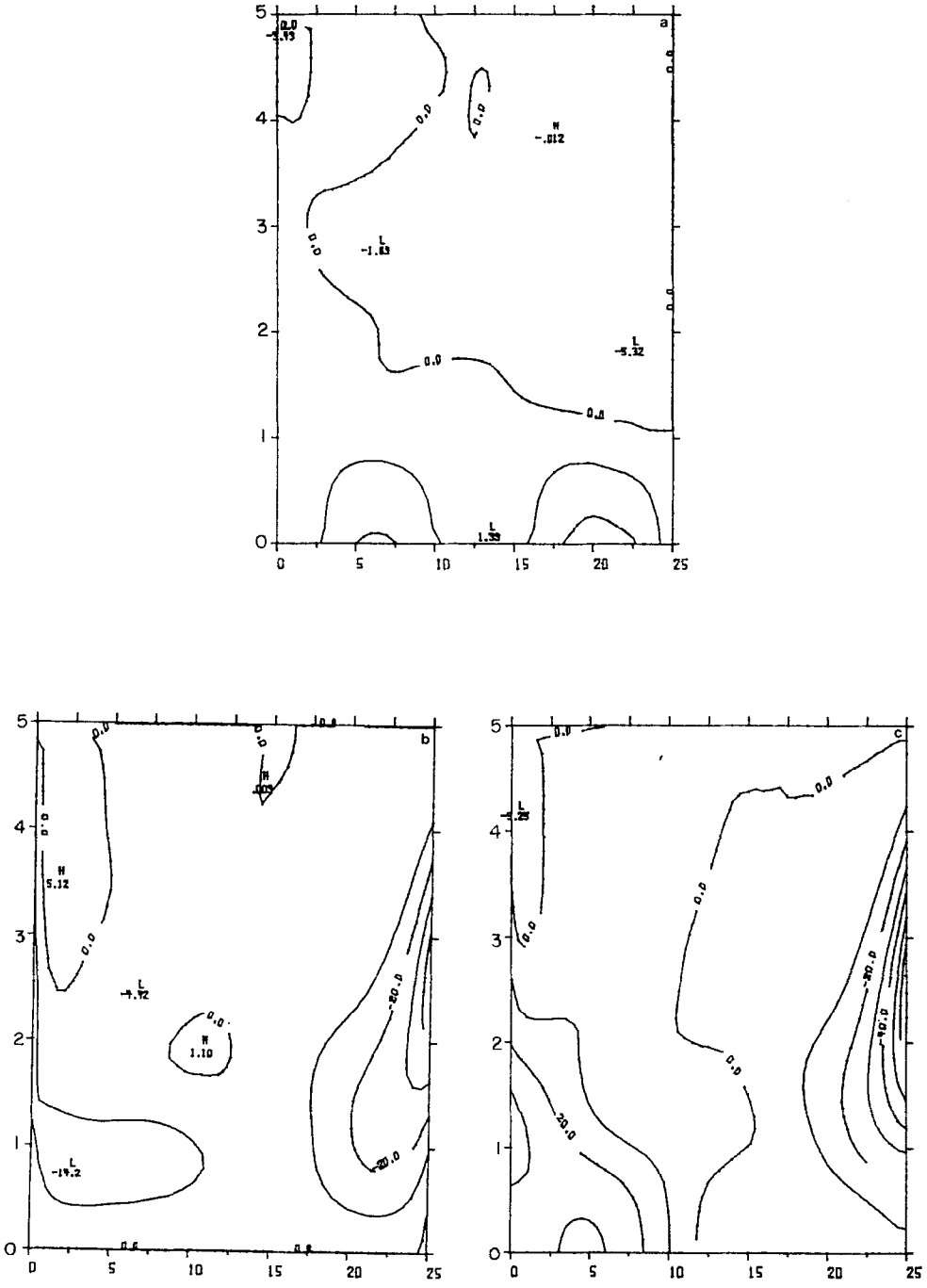

FIG. 6. Same as Fig. 5, but at time 8.0.

wave has a maximum amplitude at the equator, and decays as $\exp(-(1/2(y)^2)$ away from the equator (Fig. 5a). On the other hand, the north–south velocity, v, is identically zero, as expected (Fig. 5b) (O'Brien, *et al.* [11]).

Upon reaching the eastern boundary, part of the equatorial Kelvin wave travels poleward as a coastal Kelvin wave, and another part of it is reflected as a Rossby wave train. It is interesting to point out that, while the meridional Kelvin wave is travelling along the eastern boundary, the velocity, u, is identically zero (Fig. 6a). Furthermore, the velocity, v, has a maximum near that boundary and decays as $\exp(-xy/\alpha)$ away from that boundary (Fig. 6b). Figure 6a also shows the propagation of the internal Rossby wave, centered at $x = 20$, towards the western boundary along the equator.

The downwelled region observed in Figs. 6a and c in the western portion of the basin corresponds to an internal Kelvin wave front excited by the sudden cessation of the wind stress.

The flow along the eastern boundary may be represented approximately by the y-momentum balance:

$$\frac{\partial v}{\partial t} \approx -yu - \frac{\partial h}{\partial y}. \tag{4.1}$$

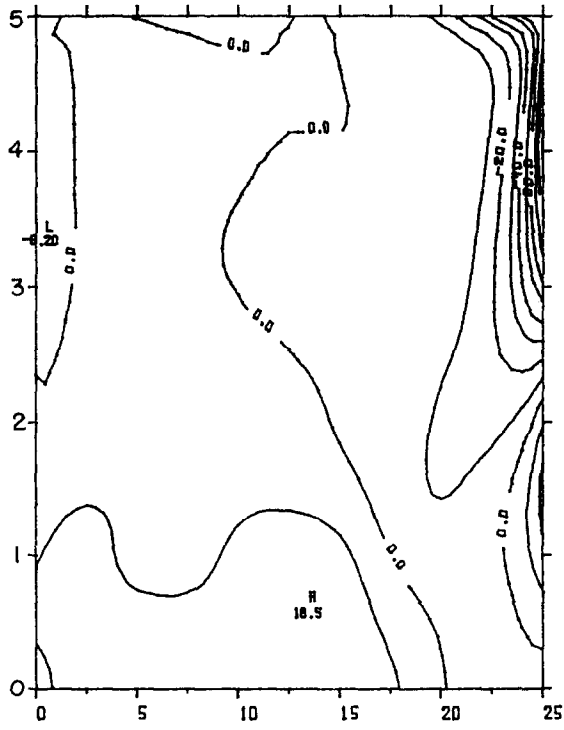

FIG. 7. Height field, at time 10.0, for the closed domain, for the first experiment.

Because u is almost negligible along the boundary, it is accurate to state that:

$$\frac{\partial v}{\partial t} \approx \frac{\partial h}{\partial y} \tag{4.2}$$

along the eastern boundary.

Figure 7 shows the upwelled region of the internal Kelvin wave front arriving at the northern boundary at time 10.0. While the coastal Kelvin wave front is moving northward, it is also transferring energy to a Rossby wave, which moves to the west (Figs. 6c and 7) at a speed of $\alpha/3$ for the gravest latitudinal mode (Hurlburt, *et al.* [7]). At time 12.0, this internal Kelvin wave front is already confined to a narrow boundary layer at the northern boundary (Fig. 8). Another interesting feature to observe at the eastern boundary at this same time is the poleward evolution of the downwelled region associated with the other internal Kelvin wave front.

In the open basin experiment, we are interested in studying the outflow of the first eastern coastal Kelvin wave front as it moves away from the equator. The three different sets of northern open boundary conditions described in the previous section are tested. In order to compare these cases with the closed basin solution, the meridional extension of the basin is shortened to $4L_y$.

The open boundary conditions I and II are tested. At time 8.0, the leading edge of

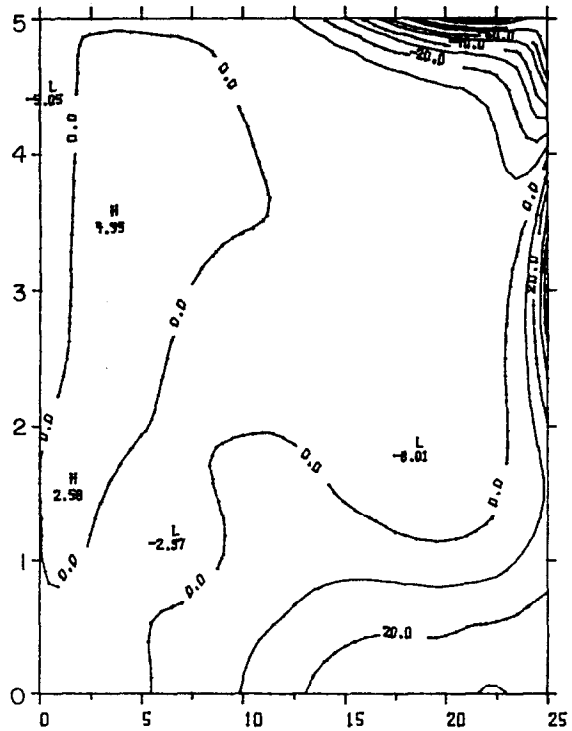

FIG. 8. Same as Fig. 7, but at time 12.0.

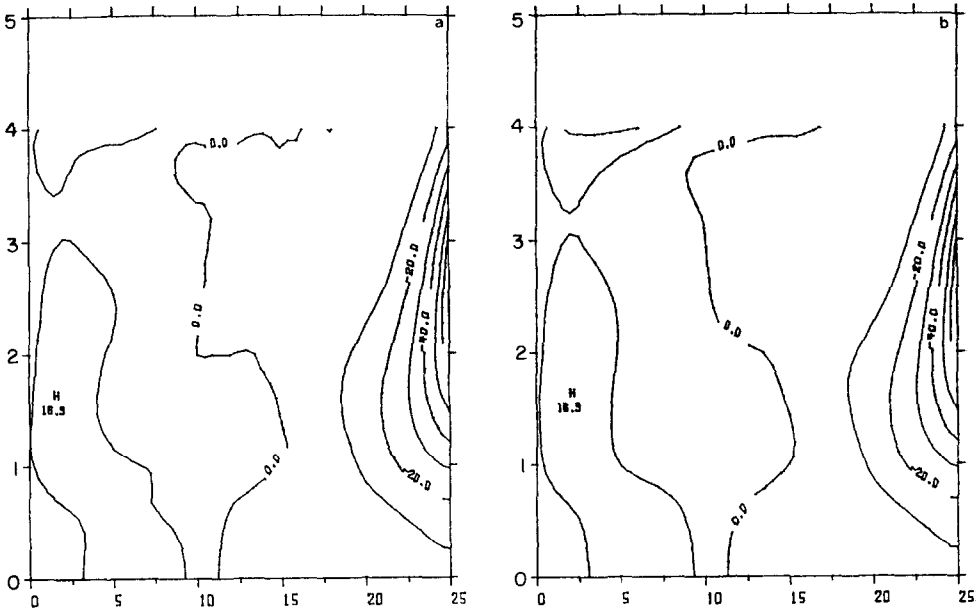

FIG. 9. Height field with boundary conditions (a) *I*, and (b) *II*, at the northern boundary, at time 8.0, for the first experiment.

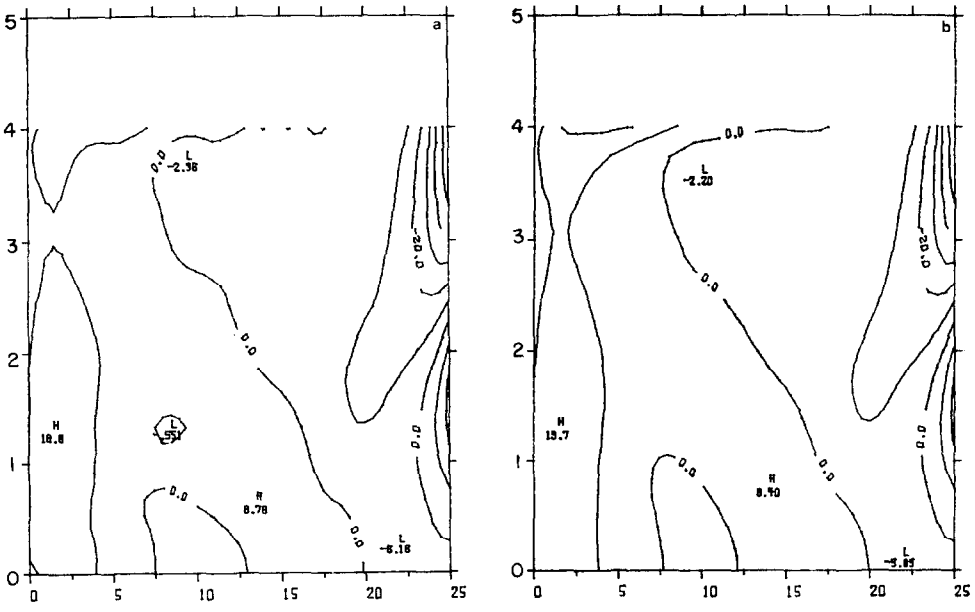

FIG. 10. Same as Fig. 9, but at time 10.0.

the coastal Kelvin wave front reaches the northern open boundary (Figs. 9a and b). A very close similarity to the closed basin solution is observed (Fig. 6c). At time 10.0, the evolution of this wave front through the open boundary (Figs. 10a and b) shows a perfect agreement with the closed basin solution (Fig. 7). At time 12.0, also in perfect agreement with the closed basin solution (Fig. 8), the coastal Kelvin wave front has already passed through the northern open boundary (Figs. 11a and b).

The other coastal Kelvin wave front, produced by the sudden cessation of the wind stress at time 4.0, is arriving at the northern boundary at time 12.0, in perfect agreement with the closed basin solution. We can conclude that in this experiment no contamination of the interior solution nor computational reflection of nondispersive waves is observed at the artificial boundary with the application of the open boundary conditions I and II. Thus, the outflow of a nondispersive wave has been successfully implemented. Both Orlanski's method and the modified technique are useful.

In the second experiment, the easterly wind imposed in the western third of the basin is applied continuously. Upon reaching the northern boundary, the meridional Kelvin wave travels along that boundary toward the west. Conservation of energy dictates that an increase in the amplitude of the coastal Kelvin wave must take place. This is related to the change of the trapping scale, which along the northern boundary is of the order of 1/5.

The aim of this second experiment is to simulate the outflow of the Rossby and the meridional Kelvin waves for the free wave problem. The closed basin solution shows the leading edge of the internal coastal Kelvin wave front, at $x = 17$, moving westward along the northern boundary (Fig. 12). The downwelled region observed in the

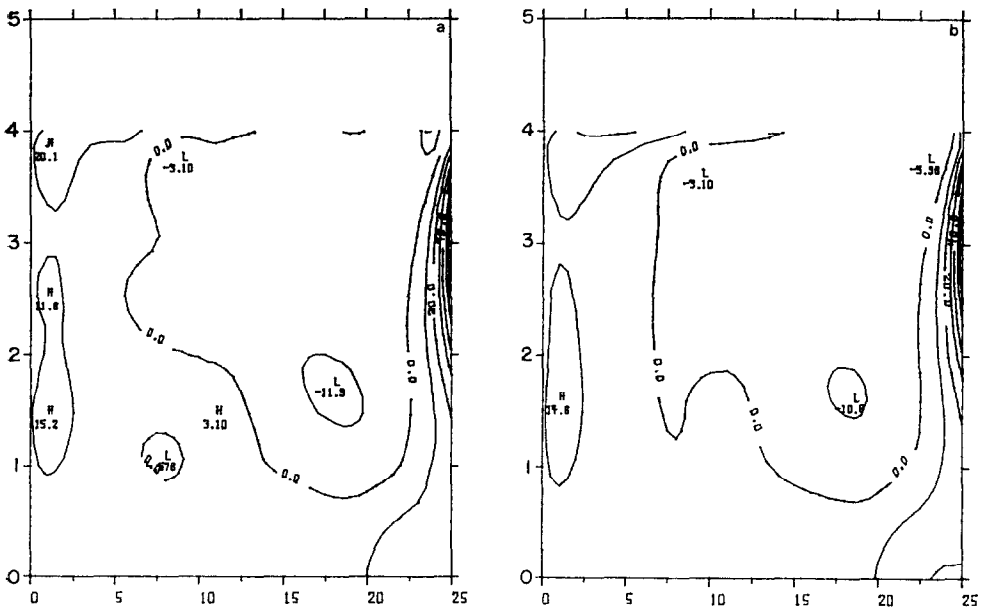

FIG. 11. Same as Fig. 9, but at time 12.0.

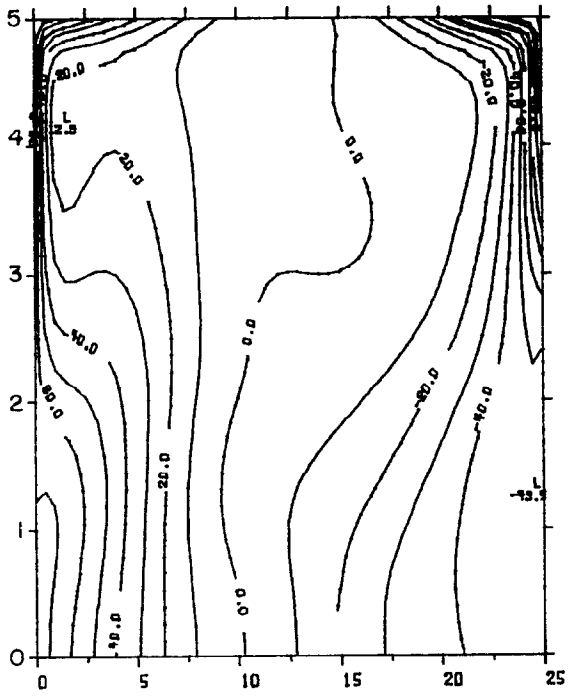

FIG. 12. Height field for the closed domain, at time 11.0, for the second experiment.

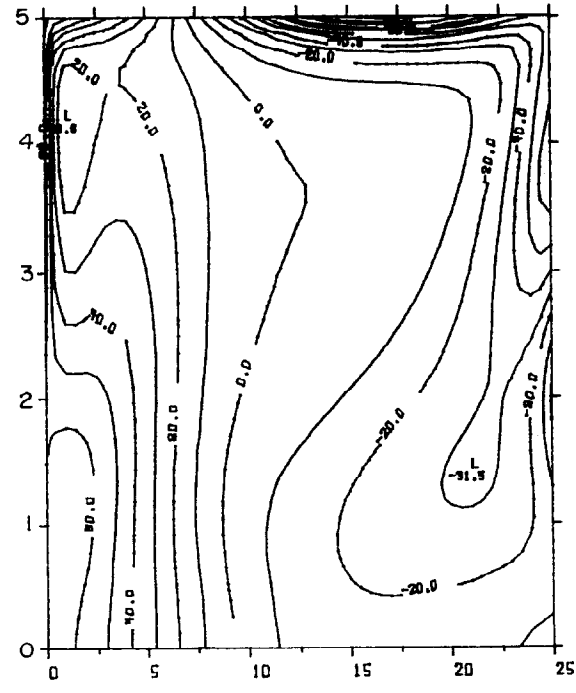

FIG. 13. Same as Fig. 12, but at time 14.0.

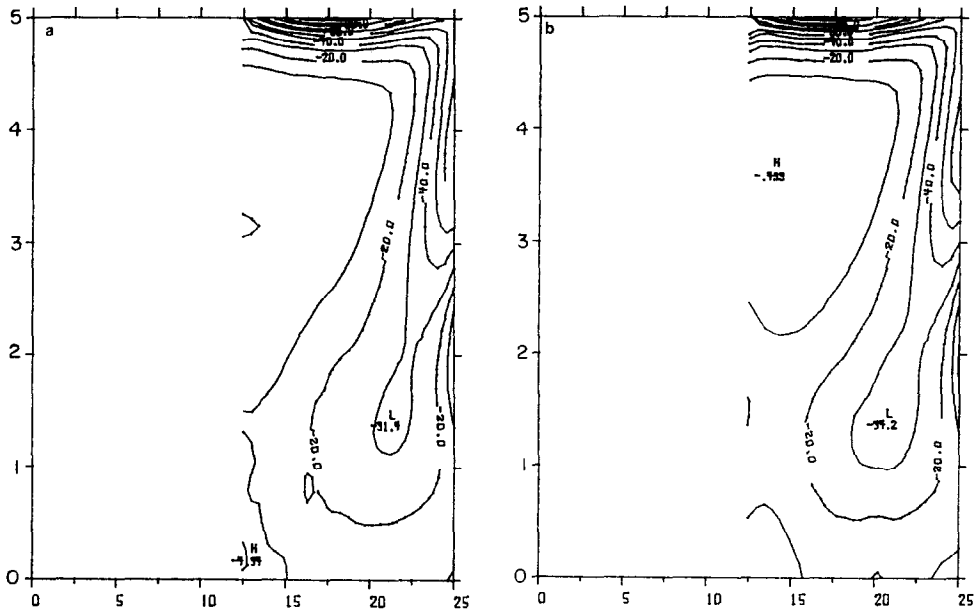

FIG. 14. Height field with boundary conditions (a) I, and (b) II, at time 14.0, for the second experiment.

western half of the basin is caused by downwelling along the northern boundary due to the easterly wind and coastal Kelvin waves which propagate counterclockwise. At time 14.0, the leading edge of the coastal Kelvin wave (Fig. 13) is located at $x = 17$. We can observe the Rossby wave, fully developed, in the eastern half of the basin. As of time 15.0, the wind is suddenly shut off, and the downwelled region starts to move eastward as an equatorial Kelvin wave. At time 16.0, we can verify this effect (Fig. 15). Meanwhile, the leading edge of the northern coastal Kelvin wave is reaching the western boundary (Fig. 15).

In the open basin case, our integration is carried out in a closed basin of solid walls of zero slip up to time 11.5. At this time, we place an open boundary in the center of the basin at $x = L/2$. Boundary conditions I and II are our new "western" boundary conditions. From $t = 11.5$, the time-integration is carried on the rectangle $0 \leqslant y \leqslant W$; $L/2 \leqslant x \leqslant L$ and compared to the larger enclosed domain.

As the effects of the remote forcing are no longer present in our foreshortened basin, one can expect a slightly different solution in these two cases as compared to those of the closed basin solution. At time 14.0, the two sets of open boundary conditions show a good agreement with the closed basin solution (Figs. 14a and b). The outflow of the coastal Kelvin wave seems to progress naturally with the implemented variation, II, of Orlanski's procedure (Fig. 16b). However, the new implemented variation, II of Orlanski's procedure shows an increasing reflection at the outflow of the Rossby wave. At this same time, the implementation of Orlanski's original boundary condition, I,

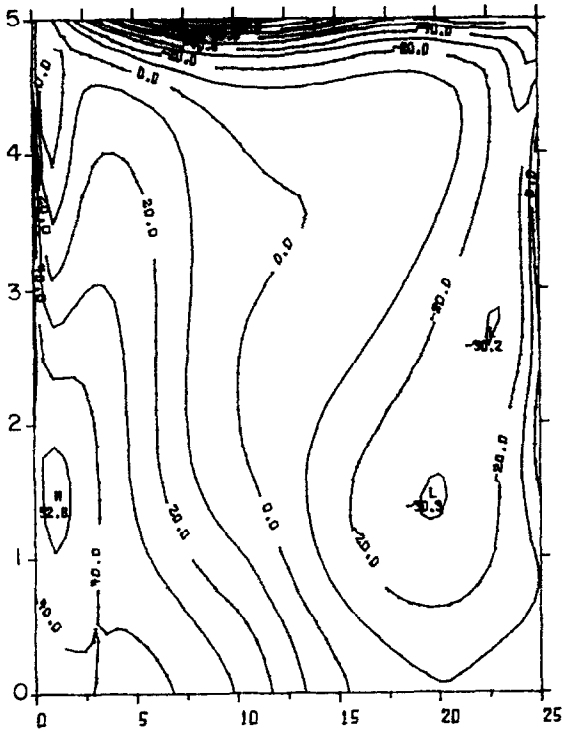

FIG. 15. Same as Fig. 12, but at time 16.0.

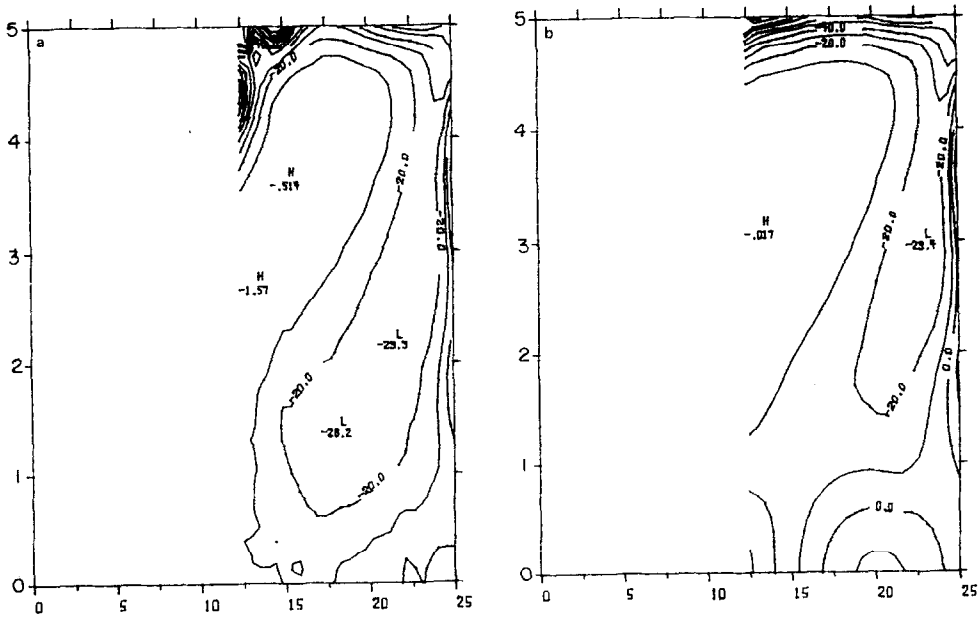

FIG. 16. Same as Fig. 14, but at time 16.0.

shows an unacceptable reflection at the outflow of the coastal Kelvin wave region (Fig. 16a). With the new implementation of Orlanski's boundary condition, we have successfully simulated the outflow of the Kelvin wave for the free wave problem. The new method is better but does not have the long-time stability that a perfect boundary condition should have.

After simulating the outflow of the Kelvin wave for the free wave problem, a more general experiment is devised. In this case, we attempt to simulate the outflow of the Kelvin wave for the forced wave problem. Only the new implementation, II, of Orlanski's boundary condition is used. For this purpose, we impose a steady (constant) stress for all the grid points during the whole period of integration. This wind stress simulates the zonal wind stress in an equatorial region. The sudden imposition of the easterly wind over all the grid points generates a different kind of physics as compared with the two previous experiments. The closed basin solution shows that along the northern boundary a downwelled region, associated with a coastal Kelvin wave front, is generated (Fig. 17). This wave front travels to the west.

The imposed stress plays a somewhat different role in the physics of the problem at the eastern boundary along the equator. Initially, a Rossby wave is excited and travels toward the west along the equator. Also, a meridional Kelvin wave front is excited. The trapping scale of this coastal Kelvin wave front changes by the factor

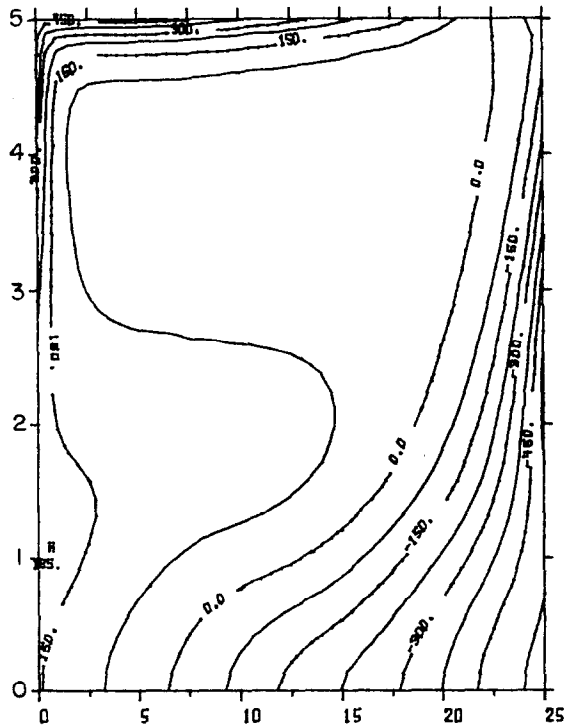

FIG. 17. Height field for the closed domain, at time 6.0, for the third experiment.

$1/y$ as it propagates northward. In other words, as the coastal Kelvin wave moves poleward, it tends to conserve energy. This has a double effect. On one hand, a Rossby wave is constantly generated; on the other hand, a decrease in the trapping scale takes place. The increase of the amplitude of the coastal Kelvin wave front, as it moves northward, is related to the latter effect. The maximum amplitude is located along that eastern boundary.

On the western side of the basin, along the equator, an internal Kelvin wave is excited, as in the previous experiments. The dynamics of this experiment differs somewhat from the previous ones. In this case, the flow along the equator is represented by the u-momentum equation:

$$\frac{\partial u}{\partial t} \approx -\alpha \frac{\partial h}{\partial x} + \delta(\tau^x/\rho). \tag{4.3}$$

In the region between the Rossby and Kelvin wave fronts, we have:

$$\frac{\partial h}{\partial x} \approx 0 \tag{4.4}$$

and, consequently:

$$\frac{\partial u}{\partial t} \approx \delta(\tau^x/\rho) \tag{4.5}$$

i.e., an easterly acceleration of the equatorial jet (Yoshida, [18]). Now, in regions where one of the two wave fronts has passed we have:

$$\frac{\partial u}{\partial t} \approx 0 \tag{4.6}$$

and consequently:

$$\alpha \frac{\partial h}{\partial x} \approx \delta(\tau^x/\rho). \tag{4.7}$$

At time 5.0, the equatorial Kelvin wave front has reached the eastern boundary. Its reflection generates a Rossby wave, which travels westward, and a coastal Kelvin wave front, which moves poleward. At time 6.0, the positions of both the coastal and meridional Kelvin wave fronts are clearly depicted (Fig. 17). The shape of the pressure gradient near the equator gives us a fairly good idea of the existence of these Rossby waves.

According to calculations, at time 6.0, the leading edge of the first Rossby wave travelling along the equator is located at $x = L/2$. Bearing this in mind, we place the new implementation of Orlanski's boundary conditions, at this point, at time 6.5. This particular time is chosen because we want to determine whether the inclusion of this computational boundary condition will in some way distort the outflow of the Rossby wave already under process.

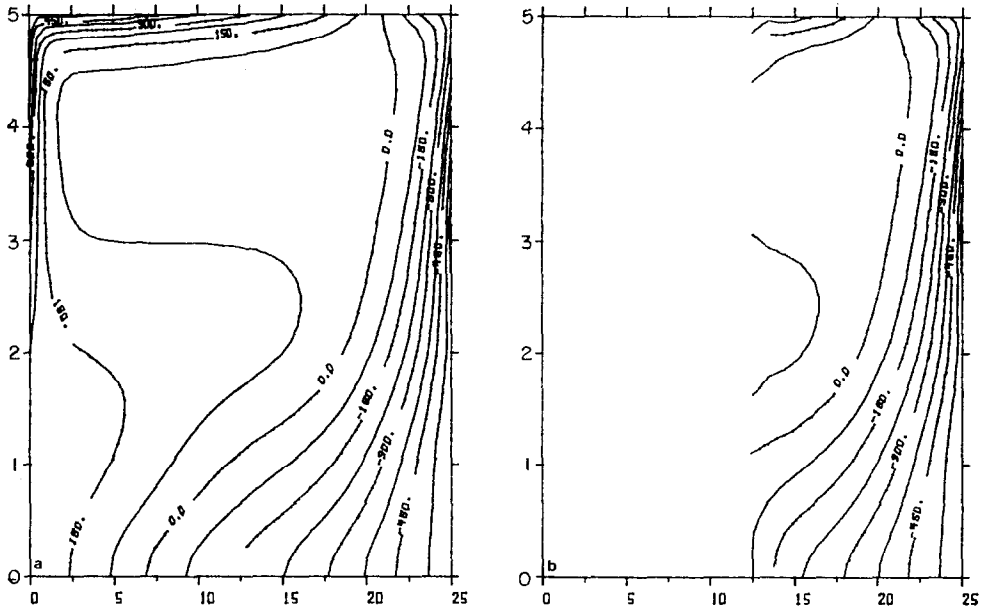

FIG. 18. Height field for (a) closed domain, (b) boundary condition II, at time 7.0, for the third experiment.

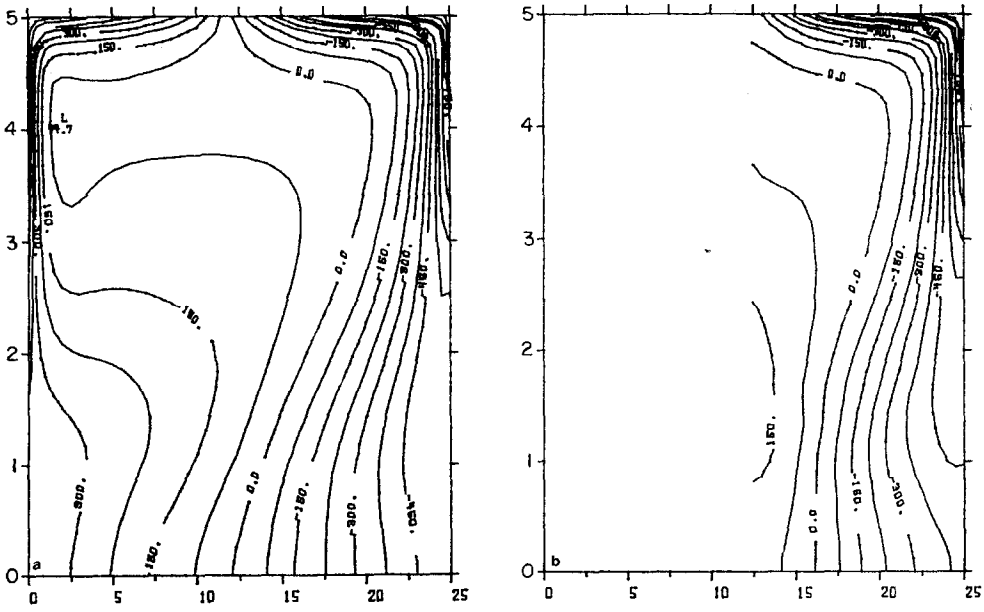

FIG. 19. Same as Fig. 18, but at time 11.0.

Although the rectangle in which the time integration is carried on is the same as in the second experiment, a constant easterly wind blows towards the "new" western open boundary during the whole period of integration. The feature we are interested in simulating in this experiment is the outflow of the northern coastal Kelvin wave.

At time 7.0, the outflow of the coastal Kelvin wave front in the open basin solution (Fig. 18b) shows a perfect agreement with that of the closed basin solution (Fig. 18a). Comparison of time 11.0 (Fig. 19b) and time 7.0 (Fig. 18b) shows that the outflow of the first northern coastal Kelvin wave front is completed in perfect agreement with the closed basin solution. At time 15.0, the open basin solution (Fig. 20b) shows that the outflow of the second northern coastal Kelvin wave is progressing normally, while the interior solution is contaminated by partial reflection of the Rossby wave at the artificial boundary.

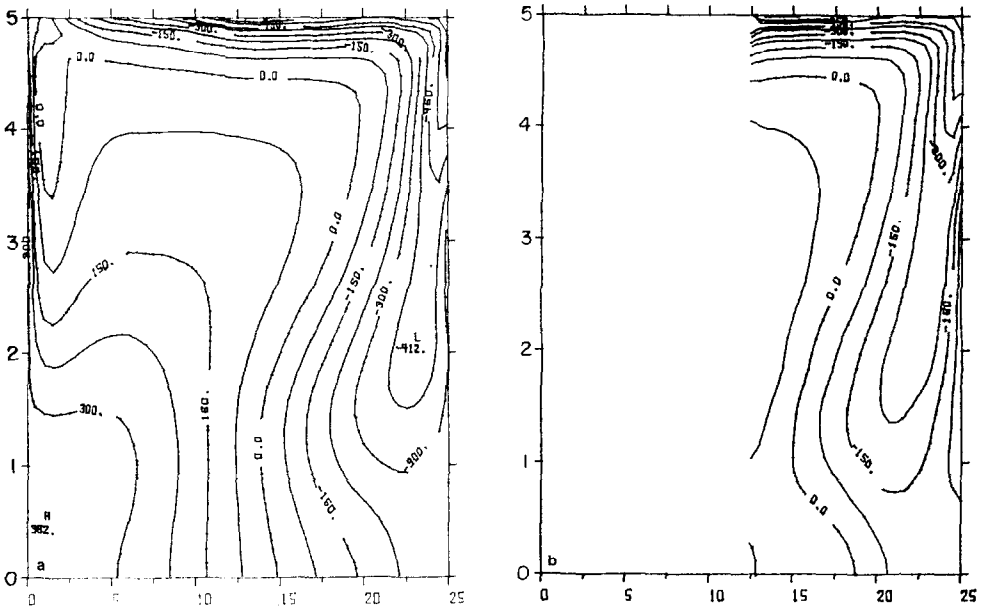

FIG. 20. Same as Fig. 18, but at time 15.0.

5. CONCLUSIONS

The aim of this investigation was to simulate the outflow of dispersive and non-dispersive waves. In our study, these waves were the Rossby and Kelvin waves, respectively. For the purpose of this investigation, the experiments were conducted with different sets of open boundary conditions. Because the linear shallow water wave equations are hyperbolic in nature, a Sommerfeld radiation condition was implemented as a prescribed open boundary.

Three severe tests were conducted to cover the whole spectrum of both the free and

forced wave problem. In the first two experiments, the free wave problem was studied. While in the third experiment the forced wave problem was studied. In the first experiment, the outflow of the eastern coastal Kelvin wave, which moves away from the equator, was successfully simulated. In the second and third experiments, the new variation, II, of Orlanski's procedure showed almost no reflection at the outflow of the northern coastal Kelvin wave. However, some reflection at the outflow of the Rossby wave was observed in both experiments with this open boundary condition. On the other hand, in the second experiment, the implementation of Orlanski's original boundary condition showed an unacceptable reflection at the outflow of the northern coastal Kelvin wave and noise in the Rossby wave region.

ACKNOWLEDGMENTS

The authors would like to thank J. J. Stephens, N. Suginohara, and I. Orlanski for their assistance. Support for this work has been provided by the Ocean Science and Technology Division of the Office of Naval Research. The computations were performed at the F.S.U. Computer Center. Partial support was derived from the CUEA/IDOE project. We would like to thank Susan Finney for typing the manuscript.

REFERENCES

1. J. G. CHARNEY, R. FJORTØFT, AND J. VON NEUMANN, *Tellus* **2** (1950), 237.
2. H. C. DAVIES, *J. Atmos. Sci.* **30** (1973), 147.
3. A. ELIASSEN, "A Procedure for Numerical Integration of the Primitive Equations of the Two-Parameter Model of the Atmosphere," Sci. Report No. 4, Dept. of Meteorology, University of California, Los Angeles, 1956.
4. B. ENGQUIST AND A. MAJDA, *Math. Comp.* **31** (1977), 629.
5. G. J. HALTINER, "Numerical Weather Prediction," Wiley, New York, 1971.
6. G. E. HILL, *J., Appl. Meteorol.* **7** (1968), 29.
7. H. E. HURLBURT, J. C. KINDLE, AND J. J. O'BRIEN, *J. Phys. Oceanog.* **6** (1976), 621.
8. T. MATSUNO, *J. Meteorol. Soc. Japan* **44** (1966), 145.
9. D. W. MOORE, "Planetary–Gravity Waves in an Equatorial Ocean," Ph.D. Thesis, Harvard University, Cambridge, Mass., 1968.
10. T. NITTA, *J. Meteorol. Soc. Japan* **40** (1962), 13.
11. J. J. O'BRIEN, D. ADAMEC, AND D. MOORE, *Geophys. Res. Lett.* **5** (1978), 641.
12. J. OLIGER AND A. SUNDSTROM, "Theoretical and Practical Aspects of Some Initial Boundary Value Problems in Fluid Dynamics," Report, Computer Science Dept., Stanford University, 1976.
13. I. ORLANSKI, *J. Comput. Phys.* **21** (1976), 251.
14. G. W. PLATZMAN, *Arch. Meteorol. Geophys. Bioklimatol. Ser. A* **7** (1954), 29.
15. R. O. REID, A. R. ROBINSON, AND K. BRYAN, "Numerical Models of Ocean Circulation," National Academy of Sciences, Washington, D.C., 1975.
16. M. A. SHAPIRO AND J. J. O'BRIEN, *J. Appl. Meteorol.* **9** (1970), 345.
17. H. WANG AND P. HALPERN, *J. Appl. Meteorol.* **9** (1970), 545.
18. K. YOSHIDA, *J. Oceanog. Soc. Japan* **15** (1956), 154.